



RESEARCH ARTICLE

10.1002/2017JB014149

Key Points:

- Shock-tube experiments characterize the effect of physical boundary conditions on pyroclast ejection
- Particle exit velocity is influenced by system geometry, particle size, and temperature
- Velocity decay is mainly influenced by particle load

Supporting Information:

- Data Set 1
- Movie S1
- Movie S2
- Supporting Information S1

Correspondence to:

V. Cigala,
valeria.cigala@min.uni-muenchen.de

Citation:

Cigala, V., U. Kueppers, J. J. Peña Fernández, J. Taddeucci, J. Sesterhenn, and D. B. Dingwell (2017), The dynamics of volcanic jets: Temporal evolution of particles exit velocity from shock-tube experiments, *J. Geophys. Res. Solid Earth*, 122, 6031–6045, doi:10.1002/2017JB014149.

Received 28 FEB 2017

Accepted 21 JUL 2017

Accepted article online 24 JUL 2017

Published online 9 AUG 2017

The dynamics of volcanic jets: Temporal evolution of particles exit velocity from shock-tube experiments

V. Cigala¹ , U. Kueppers¹, J. J. Peña Fernández² , J. Taddeucci³ , J. Sesterhenn², and D. B. Dingwell¹

¹Ludwig-Maximilians-Universität (LMU), Munich, Germany, ²Technische Universität Berlin, Berlin, Germany, ³Istituto Nazionale di Geofisica e Vulcanologia (INGV), Rome, Italy

Abstract Pyroclast ejection during explosive volcanic eruptions occurs under highly dynamic conditions involving great variations in flux, particle sizes, and velocities. This variability must be a direct consequence of complex interactions between physical and chemical parameters inside the volcanic plumbing system. The boundary conditions of such phenomena cannot be fully characterized via field observation and indirect measurements alone. In order to understand better eruptive processes, we conducted scaled and controlled laboratory experiments. By performing shock-tube experiments at known conditions, we defined the influence of physical boundary conditions on the dynamics of pyroclast ejection. If applied to nature, we are focusing in the near-vent processes where, independently of fragmentation mechanism, impulsively released gas-pyroclast mixtures can be observed. These conditions can be met during, e.g., Strombolian or Vulcanian eruptions, parts of Plinian eruptions, or phreatomagmatic explosions. The following parameters were varied: (1) tube length, (2) vent geometry, (3) particle load, (4) temperature, and (5) particle size distribution. Gas and particles in the experiments are not coupled ($St \gg 1$). The initial overpressure, with respect to atmosphere, was always at 15 MPa. We found a positive correlation of pyroclast ejection velocity with (1) particle load, (2) diverging vent walls, and (3) temperature as well as a negative correlation with (1) tube length and (2) particle size. Additionally, we found that particle load strongly affects the temporal evolution of particle ejection velocity. These findings stress the importance of scaled and repeatable laboratory experiments for a better understanding of volcanic phenomena and therefore volcanic hazard assessment.

1. Introduction

Explosive volcanic eruptions eject tephra and gas into the atmosphere at a range of velocities, posing potential hazard both in the near- and far-field. Ejected tephra and gas may form eruptive plumes that commonly comprise a gas-thrust region overlaid, when formed, by a buoyant region [Woods, 1988; Valentine, 1998]. Plume height is driven by kinetic energy and gas expansion in the near-vent region, followed by buoyancy due to the entrainment and heating of ambient air in the buoyant region [Woods, 1988; Valentine, 1998; Carcano et al., 2014]. With abundant fine ash present and a high thermal budget, an eruptive column can become buoyant if sufficient ambient air is entrained and heated to reduce the density of the gas-particle mixture to values lower than the surrounding atmosphere. If those conditions are not met, the eruptive column is prone to partial or total collapse, generating pyroclastic density currents. Valentine [1998] summarized the boundary conditions favoring buoyant rise over collapse as (1) narrow vents, (2) high exit velocities, (3) high gas content, and possibly (4) high pressure ratio at the vent. The role of vent geometry on plume dynamics during explosive eruptions has been the focus of studies investigating ejection velocity [Wilson et al., 1980; Wilson and Head, 1981; Kieffer, 1989] and jet radius [Woods and Bower, 1995; Jessop et al., 2016]. If ejection velocity is mainly determined by gas mass fraction, gas overpressure at the vent, and magma temperature [Woods and Bower, 1995], a flaring vent can help in driving the transition between subsonic and supersonic flow [Wilson and Head, 1981; Kieffer, 1989]. Furthermore, vent characteristics seem to affect the mass eruption rate (MER), as it is proportional to the cross-sectional area of the jet, which is related to the vent size [Koyaguchi et al., 2010; Ogden, 2011; Saffaraval et al., 2012; Jessop et al., 2016]. In nature, a wide range of vent geometries has been observed, from circular to elongated, and these features are dynamically evolving. Such shape changes are intrinsically related to eruption dynamics and may involve both widening (by, e.g., vent erosion and flaring) and narrowing (by, e.g., collapse, infill or accretion). At constant MER, an increase

©2017. The Authors.

This is an open access article under the terms of the Creative Commons Attribution-NonCommercial-NoDerivs License, which permits use and distribution in any medium, provided the original work is properly cited, the use is non-commercial and no modifications or adaptations are made.

in the crater diameter will influence the flow dynamics such that column collapse becomes more likely [Wilson *et al.*, 1980; Koyaguchi *et al.*, 2010]. Moreover, changes of vent geometry will also affect the flow dynamics in the underlying plumbing system. Cone buildup by near-vent deposition and partial obstruction of the crater by pyroclastic material will additionally alter flow and ejection dynamics [Capponi *et al.*, 2016].

Amount and size of the ejected particles (“volcanic cargo”) have a great impact on jet dynamics. Two-way and four-way coupling interactions between fluid (melt or gas) and particles in volcanic systems have been demonstrated theoretically [Bercovici and Michaut, 2010], numerically [Carcano *et al.*, 2014; Cerminara *et al.*, 2016], observationally [Taddeucci *et al.*, 2015], and experimentally [Burgisser *et al.*, 2005; Jessop *et al.*, 2016]. Accordingly, the commonly assumed “pseudo-gas” model for the gas-particle mixture is oversimplified in most volcanic cases. Rapid decompression experiments on porous volcanic rocks have shed light on the process of magma fragmentation and ejection [e.g., Alidibirov and Dingwell, 1996a, 1996b; Kueppers *et al.*, 2006a, 2006b; Alatorre-Ibargüengoitia *et al.*, 2010, 2011; Montanaro *et al.*, 2016], while analogue injection experiments investigated several aspects of plume dynamics [Chojnicki *et al.*, 2006, 2015; Jessop *et al.*, 2016]. Beyond volcanology, the influence of different working conditions on gas and particle velocity is of interest for an enhanced understanding of general gas dynamics [Sommerfeld, 1994; Peña Fernández and Sesterhenn, 2017] or thermal spraying [Yin *et al.*, 2016, and references therein].

This study focuses on the near-vent region, where, independently of fragmentation mechanism, impulsively released gas-pyroclast mixtures are ejected into the atmosphere following rapid decompression and gas expansion [Kieffer, 1984; Woods and Bower, 1995; Carcano *et al.*, 2013]. This takes place over a wide range of eruption styles as, e.g., Strombolian or Vulcanian eruptions, parts of Plinian eruptions, or phreatomagmatic explosions [Koyaguchi and Woods, 1996; Gouhier and Donnadieu, 2011; Taddeucci *et al.*, 2012; Scharff *et al.*, 2015]. Moreover, if sonic conditions are reached at vent exit a gas-particle jet with supersonic characteristics can form [Kieffer, 1984; Kieffer and Sturtevant, 1984; Woods and Bower, 1995; Ogden, 2011; Carcano *et al.*, 2014]. Using rapid decompression in shock-tube experiments, we investigated the ejection of a noncoupled ($St \gg 1$) gas-particle mixture varying the following parameters (Figure 1 and Table 1):

1. setup geometry (tube length and vent shape),
2. particle load,
3. starting grain size distribution (GSD), and
4. experimental temperature.

We aim at a better determination of the relative control of these parameters on mixture ejection as well as a better determination of the relation between observable eruption dynamics and the underlying conditions during an explosive eruption. Particle exit velocity, opening angle, and their dynamic evolution with time have been measured successfully [Dubosclard *et al.*, 2004; Gouhier and Donnadieu, 2011; Taddeucci *et al.*, 2012, 2015; Scharff *et al.*, 2015], but the knowledge of source conditions stays uncertain. For this reason, we are investigating tube length (=conduit length or depth of magma surface), particle load (=erupted mass) [Gaudin *et al.*, 2014], and vent geometry [Turner *et al.*, 2017].

2. Methodology

2.1. Experimental Facility

The experimental apparatus here used (Figure 1a) is an adapted version of the “fragmentation bomb” already described in Kueppers *et al.* [2006a, 2006b] and Alatorre-Ibargüengoitia *et al.* [2011] and a highly evolved model of the original fragmentation tank of Alidibirov and Dingwell [1996a, 1996b]. The apparatus is composed of a shock-tube (made of Nimonic 105 alloy) which allows for high P - T conditions (up to 100 MPa and 850°C). The total pressurized volume is 60 (setup 3) and 240 mm high (setups 1, 1b, and 2), respectively, and has an internal diameter of 26 mm (Figure 1b). The sample (using variable particle loads; see colors in Figure 1b) is placed therein without pressurized gas beneath. We incrementally pressurize the system with argon gas sealing the tube with a set of controlled-release diaphragm system. On diaphragm burst, four triangle-shaped segments of each diaphragm are bent upward and generate some internal diameter variation (between 26 and 28 mm). A pressure sensor records the pressure drop and triggers the recording system. The ejection takes place into a 3.35 m high stainless steel tank at ambient conditions. We repeated each set of conditions at least 3 times, in order to verify experimental repeatability. The experiments have been

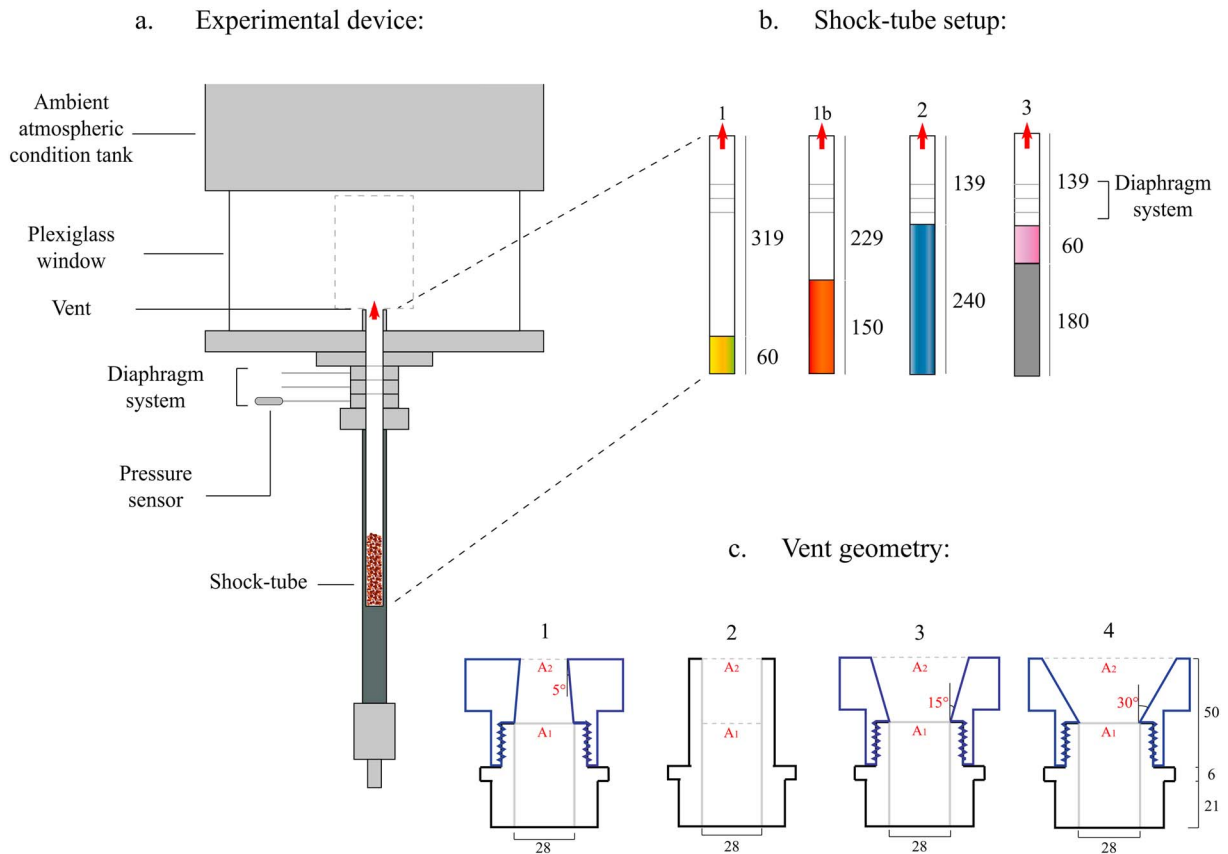


Figure 1. Overview and details of the fragmentation bomb (all values are in mm). (a) The experimental device (not to scale); the gray dot-lined rectangle in the Plexiglas window represents the camera field of view. (b) Four different starting conditions of tube length and particle load were chosen. The rectangles in color indicate the tube volume initially occupied by the granular sample (i.e., sample chamber volume in Table 1). (c) Four distinct vent geometries were used: (1) converging nozzle ($A_2/A_1 = 0.67$, A : area), (2) cylinder ($A_1 = A_2$), (3) diverging funnel 15 ($A_2/A_1 = 2.36$), and (4) diverging funnel 30 ($A_2/A_1 = 4$). The diameter of A_1 is always 28 mm.

performed during the course of >12 months with the following average conditions in the lab: 25°C, 30% humidity, and 1021.1 hPa. Through a cylindrical Plexiglas tube at the base (Figure 1a), direct visual observation and high-speed video filming are possible. A shock-absorbing panel at the top of this low- P section reduces particle loss and impact-induced fragmentation.

In this study, the primary variables were (Table 1) the following:

1. Vent geometry (Figure 1c). The following four different geometries are applied:
 - a a nozzle with converging walls ($\alpha = -5^\circ$) and area ratio $A_2/A_1 = 0.67$,
 - b a cylinder where $A_2 = A_1$,
 - c a funnel with diverging walls ($\alpha = 15^\circ$) and area ratio $A_2/A_1 = 2.36$, and

Table 1. Overview of Experimental Conditions^a

GSD (mm)	T (°C)	Setup	Distance of Sample Surface (mm)	Volume of Sample Chamber (m^3)	Particle Load ^b (g)	Vent Geometry	Exit Area (A_2) (mm^2)	Exit Diameter (mm)
1–2	25	1	319	3.2×10^{-5}	34.8 ± 2.8	Nozzle	415	23
0.5–1	500	1b	229	8.0×10^{-5}	83.0 ± 2.3	Cylinder	615	28
0.125–0.250		2	139	1.3×10^{-4}	150.9 ± 8.6	Funnel 15	1451	43
		3	139	3.2×10^{-5}	36.0 ± 3.4	Funnel 30	2462	56

^aLeft block: grain size distribution (GSD, in mm) and temperature (T , in °C). Middle block: distance of the sample surface from the vent exit before decompression (in mm), volume of the sample chamber (in m^3), and the particle load (in g). Right block: exit area (in mm^2) and exit diameter (in mm) for each vent geometry.

^bAveraged over several experiments.

Table 2. Summary of the Gas Properties for Argon, Used to Perform the Experiments, and H₂O and CO₂, Two of the Main Volcanic Gases

Gas Parameter	Ar	H ₂ O ^a	CO ₂
Specific gas constant R (J/kg/K)	208.0	461.5	188.9
Heat capacity ratio γ	1.67	1.33	1.29

^aWater vapor.

- d a funnel with diverging walls ($\alpha = 30^\circ$) and area ratio $A_2/A_1 = 4$. All of them are made from stainless steel and have a constant height (77 mm) and internal diameter (28 mm). Vent shape does not change during the experiments (not erodible), differently to other studies [Solovitz *et al.*, 2014].
- The setups (1, 1b, 2, and 3 in Figure 1b and Table 1) differ in the distance of the sample surface from the vent before decompression, and the particle load. Setups 1 and 3 have identical particle load, but different sample surface location. Setups 2 and 3 have different particle load, but identical sample surface location. Setup 1b was added to investigate the observed differences between setups 1 and 3 with setup 2. We performed setup 1b experiments only with the cylindrical vent and 25°C to check for the influence of gas flux on the observed temporal ejection velocity evolution. We chose the cylindrical geometry for standard as it is the simplest geometry and the one commonly used for eruption modeling, and we did not observe a large influence of vent geometry on the velocity evolution with time (Figure 4).
 - Sample properties. The sample is composed of fragments of basaltic lava with 15% porosity, named *Schaumlava* (SL), from the East Eifel volcanic field (Germany), produced by mechanical crushing for industrial purposes. The sample was separated by wet sieving in three different size fractions: coarse (1–2 mm, Figure A1a), medium (0.5–1 mm, Figure A1b), and fine (0.125–0.250 mm). Douillet *et al.* [2014] have measured density (2.5 g/cm³) and shape parameters. In every setup (1, 1b, 2, and 3), the loosely packed particles occupy 41.7 ± 1.8 vol %, 43.8 ± 1.6 vol %, and 50.2 ± 1.3 vol % for coarse, medium, and fine grain size distribution, respectively, irrespective of setup.
 - Two temperatures were used, 25°C (room T) and 500°C, the latter of which was achieved by using an external tube furnace. Before decompression, all particles are in thermal equilibrium with the surrounding gas phase. Upon decompression, the expanding gas phase is rapidly cooled. The degree of cooling is possibly affected by the heat capacity of the sample. This material property has been measured using a *Netzsch DSC 404C Pegasus* differential scanning calorimeter. A specific heat capacity between 830 (at low temperature) and 1000 J/kg/K (at 500°C) has been evaluated. These values are in agreement with published data for basalt [Waples and Waples, 2004].
 - We applied a gas overpressure (argon) of 15 MPa in the shock-tube for all experiments. We use argon gas to pressurize the shock-tube, assuming that the difference in its heat capacity ratio γ compared to H₂O or CO₂ is of subordinate importance (Table 2). H₂O and CO₂ are the most abundant gas species in any terrestrial eruption.

2.2. Scaling

For a close comparison of nature and experiment, it is important to compare the dynamics of the processes through a nondimensional analysis of the main controlling forces on the flow. Here we discuss Reynolds and Stokes numbers as the inertial and viscous forces dominating a momentum-driven flow, such as the flow in the near-vent region [Kieffer and Sturtevant, 1984], and to estimate the degree of coupling between gas and particles.

The flow Reynolds number (Re) defines the ratio of inertial to viscous forces in a flow:

$$Re = \frac{\rho UL}{\mu} \quad (1)$$

where ρ and μ are the fluid density and dynamic viscosity, respectively; U is the flow velocity; and L is a characteristic length, for example, the vent radius [Clarke, 2013] or the jet diameter [Kieffer and Sturtevant, 1984].

Re for volcanic eruptions ranges between 10^5 and 10^8 [Clarke, 2013] or can be as high as 10^{11} [Kieffer and Sturtevant, 1984]. The typical flow Re for our experiments ranges from 10^6 to 10^8 (Table 3), calculated using

Table 3. Summary of the Nondimensional Numbers Calculated for the Different Experimental Conditions^a

25°C	<i>M</i>		<i>Re</i>		<i>Re_p</i>		<i>St</i>	
	Exit	Throat	Exit	Fully Expanded	1–2 ^b	0.5–1 ^b	1–2 ^b	0.5–1 ^b
Nozzle	1	5.4×10^7	5.4×10^7	5.1×10^7	2.3×10^6	1.1×10^6	56	29
Cylinder	1.52	6.1×10^7	7.4×10^7	6.3×10^7	2.2×10^6	1.0×10^6	46	25
Funnel 15	2.87	6.1×10^7	1.1×10^8	9.6×10^7	2.2×10^6	1.0×10^6	31	17
Funnel 30	3.69	6.1×10^7	1.3×10^8	1.3×10^8	2.2×10^6	1.1×10^6	23	12
500°C	<i>M</i>		<i>Re</i>		<i>Re_p</i>		<i>St</i>	
	Exit	Throat	Exit	Fully Expanded	1–2 ^b	0.5–1 ^b	1–2 ^b	0.5–1 ^b
Nozzle	1	1.4×10^7	1.4×10^7	8.9×10^6	4.4×10^5	2.2×10^5	135	68
Cylinder	1.52	1.5×10^7	1.8×10^7	1.1×10^7	4.2×10^5	2.1×10^5	114	59
Funnel 15	2.87	1.5×10^7	2.1×10^7	1.7×10^7	4.1×10^5	2.0×10^5	76	40
Funnel 30	3.69	1.5×10^7	2.4×10^7	2.2×10^7	4.1×10^5	2.1×10^5	59	29

^aTheoretical Mach number (*M*) at vent exit; flow Reynolds number (*Re*) at throat, vent exit, and fully expanded conditions; particle Reynolds number (*Re_p*) at fully expanded conditions; and Stokes number (*St*) at fully expanded conditions.
^bParticle size in mm.

the one-dimensional isentropic theory [Saad, 1985; Woods, 1995] by estimating argon gas density, viscosity, and flow velocity at specific *P* and *T* values. We used the area ratio between the exit (*A*₂ in Figure 1 and Table 1) and the critical area (*A*^{*}) to estimate the flow Mach number (*M*), reported in Table 3, and therefore every other descriptive flow parameter. The critical area is defined by the narrowest cross-sectional area the flow has to pass through. In the case of this experimental setup, for the cylinder, funnel 15, and funnel 30 geometry the critical area is the sample chamber area, with a diameter of 26 mm and therefore *A*^{*} = 531 mm². The exit (*A*₂) to critical (*A*^{*}) area ratio are 1.16, 2.73, and 4.64 for the cylinder, funnel 15, and funnel 30, respectively. As a result, the exit *M* number is >1 for these geometries (Table 3). On the other hand, in the nozzle vent the critical and exit area are the same; this provides *M* = 1 at the exit. The equation used is expressed as follows and was resolved for *M* [Saad, 1985]:

$$\left(\frac{A_2}{A^*}\right) = \left(\left(\frac{2}{\gamma+1}\right)^{\frac{\gamma+1}{2(\gamma-1)}}\right) \frac{1}{M} \left[1 + \left(\frac{\gamma-1}{2}M^2\right)\right]^{\frac{\gamma+1}{2(\gamma-1)}} \quad (2)$$

Although *Re* is a highly dynamic parameter, we estimated it for throat, lip of the vent, and at fully expanded conditions, reached when the flow has expanded to ambient pressure. As characteristic length (*L*), the diameter of the vent at the throat, for throat conditions, and at its upper end, for lip, and fully expanded conditions, was chosen accordingly.

The Stokes number (*St*) describes the particle inertial response to the flow, and it is calculated as follows:

$$St = \frac{\tau_p U}{L} \quad (3)$$

where τ_p is the characteristic relaxation time of the particles and it is calculated from equation (4) [Elghobashi and Truesdell, 1993; Carcano et al., 2013]:

$$\tau_p = \frac{\rho_p d_p^2}{0.33 Re_p \mu} \quad (4)$$

where ρ_p is the particle density, d_p is the particle diameter, μ is the fluid dynamic viscosity, and *Re_p* is the particle Reynolds number. *Re_p* serves as correction factor accounting for relative velocities between gas and particles. *Re_p* is calculated according to equation (5):

$$Re_p = \frac{d_p \rho |U - u_p|}{\mu} \quad (5)$$

where u_p is the measured particle velocity and *U* is the flow velocity theoretically estimated for the fully expanded conditions using equation (6) from the one-dimensional isentropic theory [Saad, 1985; Woods, 1995]. The experimental apparatus does not allow for measuring directly the flow velocity of the pure gas,

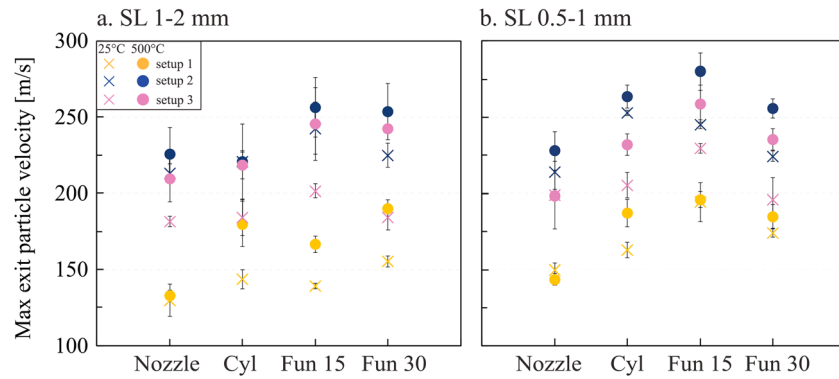


Figure 2. Maximum particle exit velocity plotted against vent geometry (Cyl = cylinder, Fun 15 = Funnel with 15° opening angle, and Fun 30 = 30° opening angle) for particles (a) 1–2 mm in size and (b) 0.5–1 mm in size. Each point and relative error bar represent the average value of velocity and standard deviation, respectively, of at least three repeated experiments at the same initial conditions. The dots are for 500°C experiments and the crosses are for room T. The error bars can be smaller than related symbol.

U. We measured the propagation velocity of the condensed gas front directly above the vent from image analysis. As there are measurement ambiguities and large variations (e.g., 366 ± 67 m/s), we decided to stick to theoretical values.

$$U = \left[\frac{2\gamma RT_0}{\gamma - 1} \left(1 - \left(\frac{P_\infty}{P_0} \right)^{\frac{\gamma-1}{\gamma}} \right) \right]^{1/2} \tag{6}$$

where T is the temperature and P is the pressure. The subscript 0 indicates the conditions in the tube prior to decompression, while subscript ∞ indicates the ambient conditions and R is the gas constant. In our observation window (Figure 1), where particle velocities were measured, St was found to be 17–135 (Table 3), meaning that gas and particles are not coupled. In theoretical studies, particles bigger than 0.5 mm are not coupled with the gas phase [Woods, 1995; Carcano et al., 2013, 2014]. In the case of experiments with particles of 0.125–0.250 mm, particles should be better coupled with the gas phase. However, low particle resolution prevents direct measurement of particle velocity (see Movie S2 in the supporting information).

2.3. Data Recording

We recorded the experiments with a Phantom high-speed camera (V710 and V711) at 10,000 fps. The field of view (resolution of 800 × 600) is 20 cm high. We used MTrackJ, an ImageJ plug-in, to manually track single particles and measure their velocity. For the fine particle fraction, manual tracking of single particles was not possible, and therefore, data on the velocity for these experiments are not available. We evaluated velocity by measuring the distance of single particles in five consecutive scaled frames and averaging the velocity for this time interval. We could detect no perceptible acceleration or deceleration. We tracked up to 40 particles per video covering the entire duration of particle ejection at a resolution of 30 frames. The particle ejection lasted between 30 and 100 ms, with the shortest being the setup 3 ejections with fine particles, from when the first particles exit the vent until particle ejection ceases.

3. Results

A predetermined rupture of the diaphragms initiated each ejection, i.e., gas and particles acceleration out of the tube. In all runs the gas, visible thanks to condensation under the illumination, preceded the first particles into the camera field of view by 1 to 5 ms, depending on the setup. Then, the particles are ejected over a variable amount of time and with specific patterns of changing ejection velocity over time.

3.1. Maximum Particle Exit Velocity

Differences in particle exit velocity (PEV) are shown as a function of tube length, vent geometry, particle load, grain size, and temperature. Maximum values are always attained at ejection onset. Values range from 130 to 300 m/s and are influenced by several parameters (Figure 2). The strongest influence is exacerbated by the

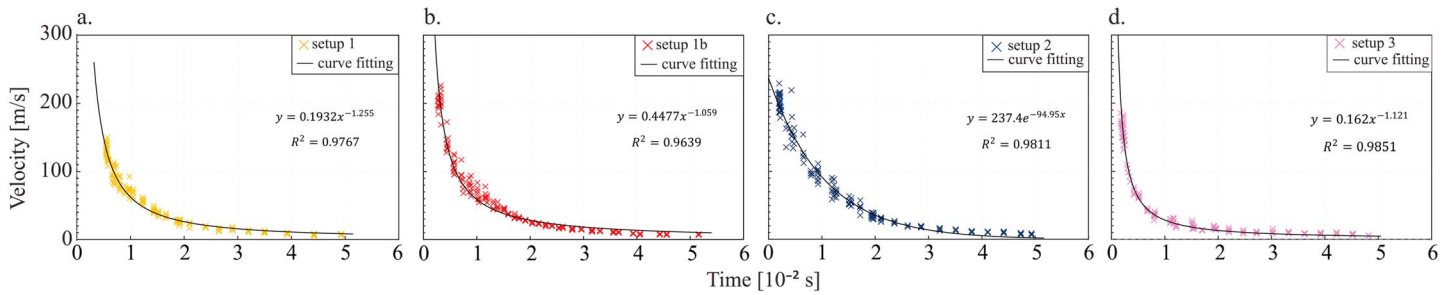


Figure 3. Temporal evolution of particle exit velocity at the vent for SL particles of 1–2 mm, initial overpressure of 15 MPa, 25°C temperature, and cylindrical vent. (a) Setup 1, (b) setup 1b, (3) setup 2, and (d) setup 3. Time zero is defined as the first appearance of condensed gas in the video, particles following after variable delay. See also Movie S1 in the supporting information.

tube length; absolute values may vary by up to 80%, followed closely by particle load (up to 60%), then vent geometry (up to 30%) and temperature (up to 25%). Grain size shows the smallest apparent contribution to the particle exit velocity (up to 20%).

3.2. Temporal Evolution of Particle Exit Velocity

Particle ejection lasted for maximum approximately 100 ms in all experiments. After 20–30 ms, the velocity decay function was found to be asymptotic toward zero for all setups and is accordingly not shown. Figure 3 representatively shows the results for experiments with SL 1–2 mm particles, performed at 15 MPa, room temperature (~25°C), and with the cylindrical vent. Time zero in the charts corresponds to the first appearance of condensed gas, which is followed by the particles with a certain delay depending on the setup (from 1–2 ms for setups 1b and 2 to 3–5 ms for setup 1). The temporal evolution of the velocity of particles during each experiment shows a nonlinear decay which is strongly controlled by the particle load and tube length. Particle exit velocity at the vent decays most rapidly for setup 3 (Figure 3d) and most slowly for setup 2 (Figure 3c). The velocity decay in setups 1, 1b, and 3 is well approximated by a power law equation, while in setup 2 it is better approximated by an exponential equation.

In order to quantitatively compare the results of the different geometries, their time velocity data points have been fitted with the best fitted curve obtained for the cylindrical geometry (Figure 4). This way, velocity deviations caused by the vent geometry are more easily observable. In some cases, measured velocities are higher or lower compared to the cases with cylinder. In general, the temporal ejection velocity evolution is strongly nonlinear for all setups with a noticeably different decay for setup 2. Setups 1, 1b, and 3 are reasonably similar and show a minor influence of vent geometry. Results of setup 2 and a nozzle vent (Figure 4e) show the strongest variation from the other three vent geometries (Figures 4f–4h). Overall, particle size and temperature do not affect the velocity decay trend significantly.

We summarize the coefficients, fitting exponents, and R^2 values for the fitting equations of experiments performed with the cylinder vent in Table 4.

The results of experiments performed at 500°C and with 0.5–1 mm particles are in Appendix A.

4. Discussion

Controlled laboratory experiments allow outlining the influence of geometrical and physical parameters on gas-particle jet dynamics. Magma inside a conduit exhibits strong horizontal and vertical gradients in its textures, mainly porosity, pore shape, and permeability [e.g., Kueppers and Wadsworth, 2015]. We performed the experiments with loose fragments of monomodal GSD (Figure A1) with a porosity of approximately 15%. Such way, the influence of energy consumption by sample fragmentation is minor [Kueppers et al., 2006b], and the observed features can be directly related to the starting conditions as (1) geometry, (2) tube length, (3) particle load, (4) temperature, and (5) GSD. Inside the tube, upon decompression, gas is expanding and accelerating uniaxially. The associated gas flux inside the sample is above the value of permeable gas flow possible even in such loose particles. According to a permeability (k) model for granular material of monodisperse size distribution [Wadsworth et al., 2016], k is about $10^{-8.4}$ m² for particles of 1–2 mm and 10^{-9} m² for

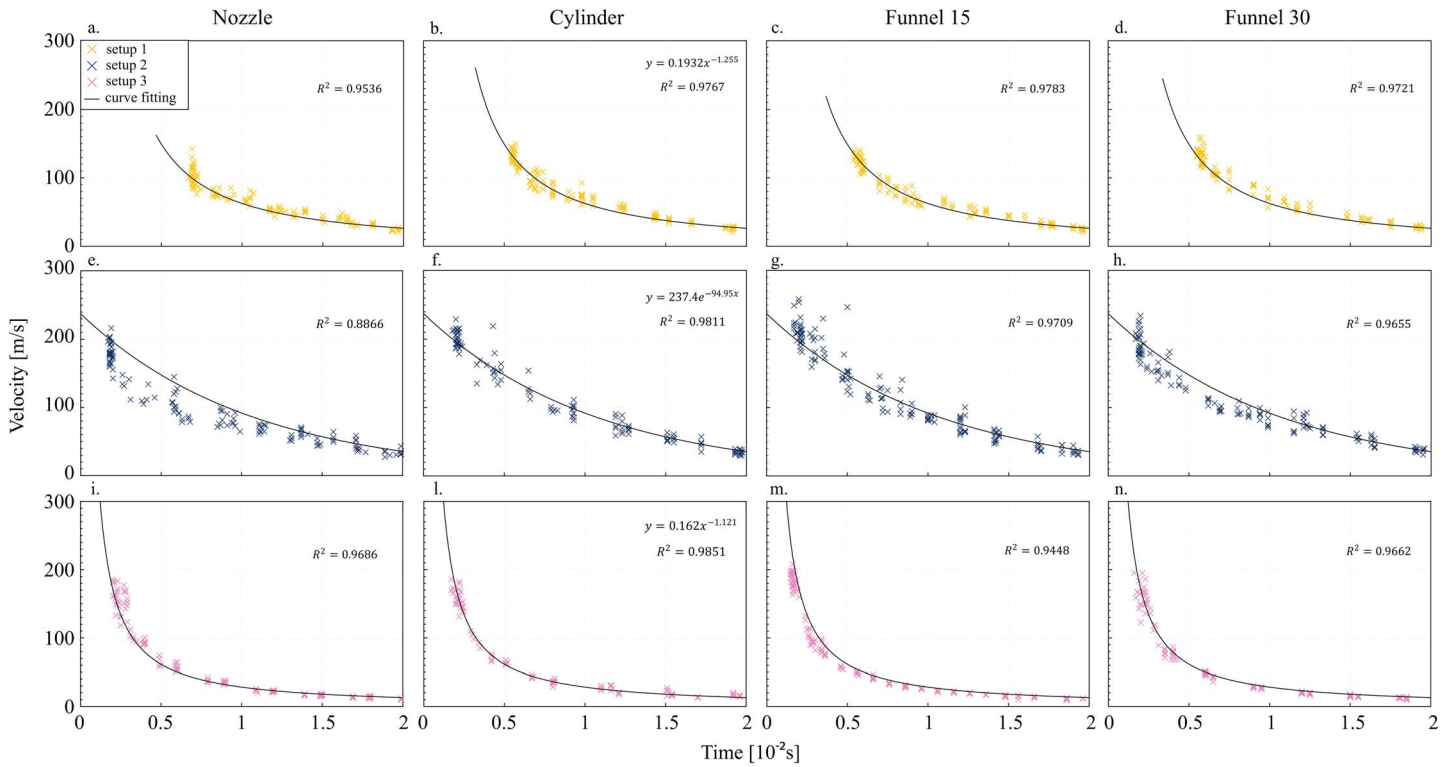


Figure 4. Temporal evolution of particle exit velocity shown for the four different vent geometries and the three setups (starting conditions: SL 1–2 mm particles, 15 MPa, 25°C). The best fit curve of the cylinder geometry is superimposed on the data from the other three geometries showing the effect of vent geometry on particle velocity decay. The error bars are not plotted in this chart, but the values of standard deviation for each point are taken into account to weight the goodness of the fitting model.

particles of 0.5–1 mm, respectively. Therefore, particles will be set in motion, coupling and acceleration of particles with and by the gas scale with particle size, shape, and density, and with gas flux and the residence time of the particles in a gas stream. After leaving the high-pressure autoclave from the vent, gas expansion is still axisymmetric, but no longer unidirectional; friction with the surrounding air begins to decelerate the jet and gas-particle coupling dynamics change.

Overall, experiments with a converging nozzle showed the lowest peak velocity values while the funnel 15 vent consistently showed the fastest values of exit velocity. These trends can be explained by gas expansion dynamics. In all experiments, the gas flow is initially supersonic because of the high-pressure ratio between

Table 4. Summary of the Best Fitting Equation Values (Coefficient, Exponent, R^2) and Maximum PEV for Experiments Performed With the Cylinder Vent And Setup, Temperature, and GSD as Listed in the Table

Setup	Temperature (°C)	GSD (mm)	Coefficient of Fit Equation	Fitting Exponent	R^2	Maximum PEV (m/s)
1	25	1–2	0.193	–1.255	0.977	144
1b	25	1–2	0.448	–1.059	0.964	220
2	25	1–2	237.4	–94.95	0.981	221
3	25	1–2	0.162	–1.121	0.985	184
1	500	1–2	0.161	–1.239	0.988	180
2	500	1–2	225.8	–97.82	0.965	221
3	500	1–2	0.145	–1.139	0.989	219
1	25	0.5–1	0.198	–1.263	0.970	163
1b	25	0.5–1	0.514	–1.053	0.927	237
2	25	0.5–1	265	–96.8	0.978	253
3	25	0.5–1	0.135	–1.185	0.968	206
1	500	0.5–1	0.058	–1.466	0.982	187
2	500	0.5–1	265.5	–120.1	0.971	264
3	500	0.5–1	0.094	–1.231	0.991	232

the overpressurized reservoir (P_r) and the external atmospheric conditions (P_e). Additionally, the vent geometry will affect the flow (see equation (2)) [Saad, 1985; Yin *et al.*, 2016]. The nozzle vent has an exit-to-critical-area ratio of 1. Therefore, the gas accelerates until reaching sonic conditions at the exit ($M = 1$; Table 3). Afterward, the gas is free to expand further. On the other hand, the cylinder and the funnel-shaped vents have an exit-to-critical-area ratio larger than 1 and the gas can expand to supersonic velocity at the exit ($M > 1$; Table 3). However, this highly depends on the exit pressure ratio. The necessary pressure ratio is given by the following equation and depends on γ of the gas:

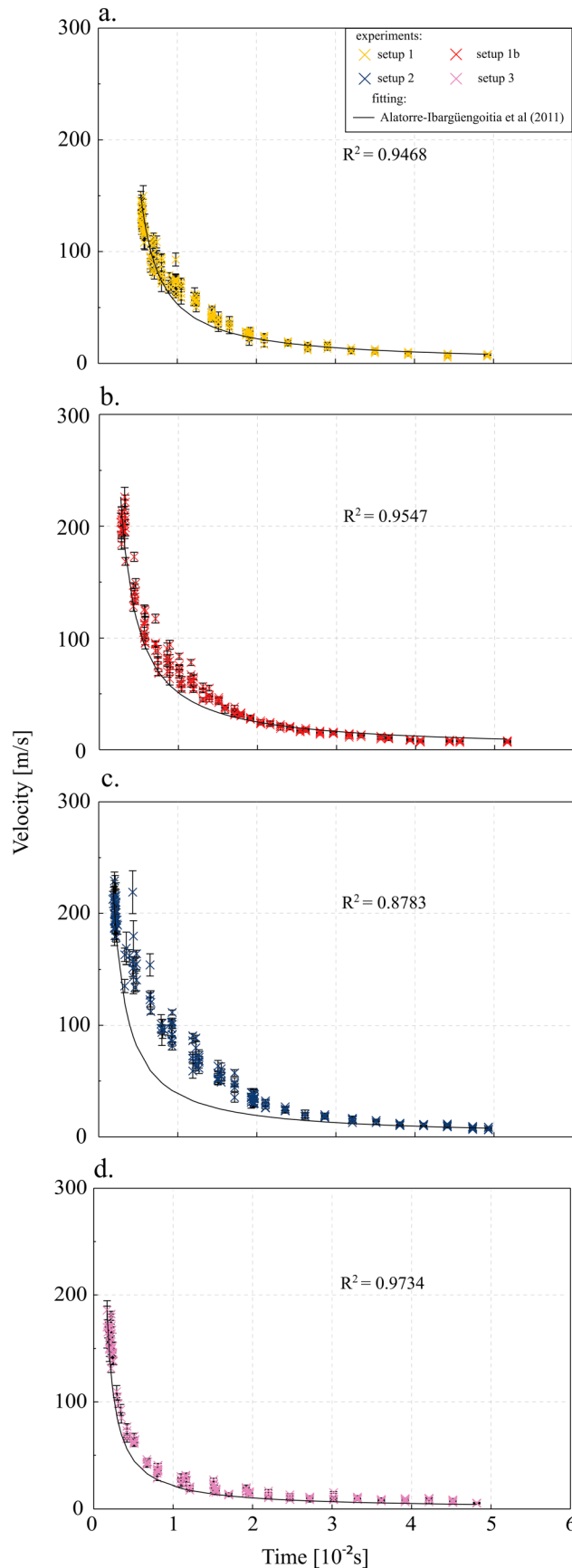
$$\frac{P_r}{P_e} = \left(1 + \frac{(\gamma - 1)M^2}{2} \right)^{\frac{\gamma}{\gamma - 1}} \quad (7)$$

Above a certain minimum pressure ratio, there is a positive correlation of the exit-to-critical-area ratio and M at the exit (equation (7)). The M values in Table 3 are the “designed” ones for the vent geometries in use, under the assumption that at ejection onset the pressure ratio, expressed by equation (7), is high enough [Saad, 1985]. Stated this, the nozzle vent, with an exit-to-critical-area ratio of 1, provides $M = 1$ (equation (2) and Table 3) if the reservoir to exit pressure ratio is at least 2, while the cylinder with an area ratio of 1.16 provides $M = 1.5$ if the pressure ratio is at least 4.2. Funnel 15 has an area ratio of 2.73, which gives $M = 2.8$ if the pressure ratio is at least 26.8. Funnel 30 has an area ratio of 4.64, which means a designed M of 3.7 if the pressure ratio is at least 72. The particles do not leave the tube instantaneously at diaphragm burst; hence, for the time the particles leave the tube and we can measure their velocity, the pressure ratio drops until a value that might be below the necessary one to have supersonic flow. Seeing the PEV values, we argue that the pressure ratio at particle exit from nozzle, cylinder, and funnel 15 did not drop yet below the necessary one when particles exit. On the other hand, the pressure ratio from funnel 30 seems to have already dropped to a value below the necessary one, and therefore, the acceleration efficiency for this geometry is lower than, for example, the one of the funnel 15.

In addition, we can argue than for all the experiments performed with setup 1, independently of vent geometry, the pressure ratio at the vent has already dropped below supersonic conditions at the onset of particle ejection.

Temperature has a positive correlation with particle velocity. A higher temperature means that for fixed volume and pressure, a smaller amount of gas (in moles) is filling the reservoir. On the other hand, the speed of sound of the gas flow greatly depends on temperature ($c^2 = \gamma RT$, where c is the speed of sound, γ is the gas heat capacity ratio, R is the gas constant, and T is the temperature). Accordingly, a higher temperature produces a larger speed of sound ergo particles that are accelerated more even if less gas is available. Furthermore, we observed that smaller particles exhibit higher velocities than larger ones. This result can be explained by the better coupling of smaller particles with the gas flow, e.g., smaller *St*. Yin *et al.* [2016] reported similar findings for temperature and particle size effects in cold spraying empirical tests using spherical or irregular particles of metallic composition (Al, Cu), tens of micrometers in size.

In addition to the maximum exit velocity, the temporal evolution of particle exit velocity measured at the vent is different as a function of the initial conditions, in particular, tube length and particle load (Figures 3 and 4 and Appendix A). At constant particle density and size and applied overpressure, the acceleration of the particles by drag exerted by the expanding gas phase is comparable for all four setups and quasi-instantaneous. Accordingly, the observed difference in exit velocity is a direct consequence of travel path length before leaving the vent. No significant deceleration of individual particles could be measured above the vent within our field of view. Consequently, the observed difference in maximum exit velocities, and the different decay curve (power law versus exponential), is attributed to a dynamic evolution of the pressure gradient inside the shock-tube, with a negative correlation of pressure gradient and tube length. At the high-pressure gradient, the sample has no time for outgassing by permeable gas flow. Rather, the gas will set the particles in motion, thereby increasing the average particle-particle distance and bulk permeability. As a consequence, particles that were initially in the upper part of the sample will experience acceleration not only by the expanding gas that was initially “in their vicinity” but also by gas that had been stored in the lower parts of the sample. This is clearly manifested by setup 2 and to a lesser degree (for a shorter amount of time) by experiments with 1b. Initially, gas velocity will be higher than particle velocity and consequently accelerate particles according to their shape and surface roughness. Once the gas has decompressed, particles will



overtake the gas because of their inertia, as observed during Strombolian eruptions [Taddeucci et al., 2015]. Similar velocity decay trends have also been reported for pyroclast ejections on different volcanoes [Dubosclard et al., 2004; Gouhier and Donnadieu, 2011; Taddeucci et al., 2012; Scharff et al., 2015].

Moreover, we recognize a smaller but systematic influence of vent geometry on velocity decay. In order to “visualize” the results, we used the best fit curve of the cylindrical vent, as a standard, for all four vent geometries per setup and calculated the R^2 values (Figure 4, Appendix A, and Table 4). The variations are minor for cylinder and funnel geometries but substantial for the converging nozzle with setup 2. The latter, having a smaller critical area and therefore a smaller rate of discharge, has the strongest effect of gas expansion behavior and accordingly particle acceleration.

Gas-pyroclast jets in nature are the first, direct observable result of the hidden process of magma fragmentation below the surface [Dubosclard et al., 2004; Gouhier and Donnadieu, 2011; Taddeucci et al., 2012; Scharff et al., 2015]. Scaled and repeatable laboratory experiments can help in shedding light on the physical processes inside a volcano. One goal is to constrain the depth of the magma surface and the effective overpressure. The observed velocity evolution of laboratory experiments was used to develop an empirical relationship [Alatorre-Ibargüengoitia et al., 2011]:

$$v_p = \frac{v_{max}}{1 + \frac{v_{max}}{h} t} \quad (8)$$

where t is the time, v_{max} is the maximum ejection velocity measured, and h corresponds to the base of the sample in the autoclave. Taddeucci et al. [2012]

Figure 5. Particle velocity decay with the curve fitting from Alatorre-Ibargüengoitia et al. [2011]. The error bars can be smaller than related symbol.

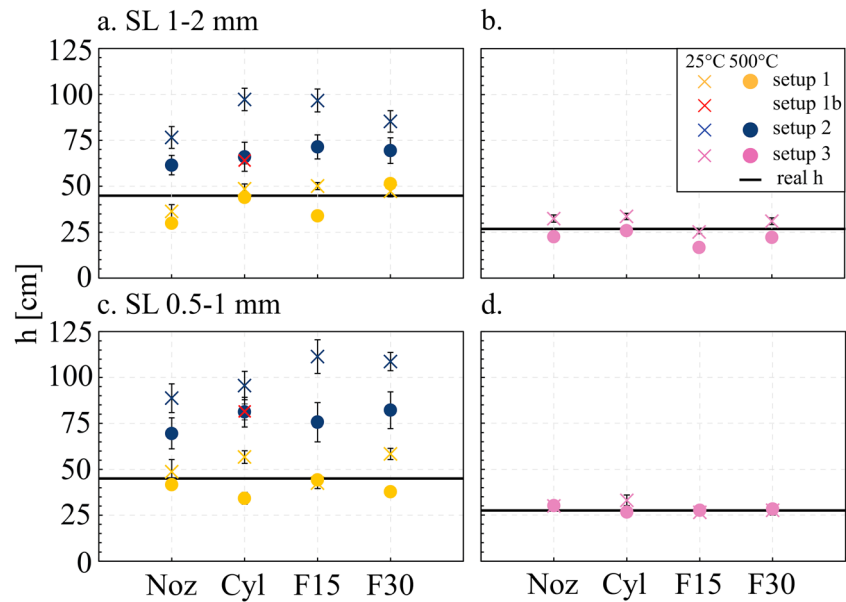


Figure 6. Values of h expressed in centimeter versus vent geometry for the different setups and particle size: (a and b) coarse fraction and (c and d) medium fraction. The horizontal black line is the real h (in the experiments), while the data points are the predicted h based on equation (8). Figures 6b and 6d show a relative lower h location; this is only because in setup 3 the total length of the conduit is actually shorter (see Figure 1 for reference).

applied this formula to short-lived volcanic explosions (exploding gas slug in Strombolian explosions) to define the base and volume of ascending gas slugs. In our experiments, we varied the position of the base of the sample as well as particle load and tested the fitting of the results with equation (8) (Figure 5). For this, we used the known h (black line in Figure 6) and the measured maximum ejection velocity to derive v_p . R^2 values range from relatively satisfactory (setup 1 ($R^2 = 0.9468$), 1b ($R^2 = 0.9547$), and setup 3 ($R^2 = 0.9734$)) to a substantial misfit for setup 2 ($R^2 = 0.8783$), primarily because exit velocities (between 3.5 and 23.5 ms after t_0) are significantly higher than predicted. Assuming h unknown, we used equation (8) to calculate it based on the known velocity decay. We find that h can be reasonably predicted for setups 1 and 3, while it is overestimated for setups 1b and 2 (Figure 6). In addition, there is no strong indication of better estimation of h with vent geometry, particle size, or temperature.

In setups 1b and 2, the particle column is up to 3 times longer compared to setups 1 and 3 (Figure 1). Two of the fundamental assumptions in equation (8) is that pressure is uniform and particle velocity is constant in the conduit [Alatorre-Ibargüenogitia et al., 2010, 2011; Taddeucci et al., 2012], or, at least, that the particle acceleration phase has the same duration [Gaudin et al., 2014]. As discussed above the length of the particle-filled conduit in setups 1b and 2 is likely enough to have differences in the pressure gradient that accelerates the particles, thus pushing the system away from the applicability of equation (8)). It follows that using equation (8) to infer eruption properties may give relative errors in h as large as 100% if the equation fit to the observed velocity decay in time shows a R^2 less than about 0.95, in particular when the misfit is toward higher than predicted velocities. However, such misfit, or, in other terms, a shift of the decay curve from a power law to an exponential function, may reveal changes of the acceleration pattern of pyroclasts during the eruption. This information is potentially important, hinting, e.g., at unsteady pressure gradients within the conduit or nonnegligible effects of permeable gas flow.

5. Conclusions

We have investigated the complex dynamic processes and two-way interactions taking place in shock-tube experiments. These experiments mimic processes in the conduit and the near-vent region during explosive eruptions. Through the evaluation of empirical relationships, a better understanding of the underlying processes of directly observable, natural volcanic eruptions will be possible. The results may aid in understanding the development of buoyant eruption plumes [Tournigand et al., 2017].

Given the experimental conditions, the present results indicate that—in decreasing importance—tube length, particle load, vent geometry, temperature, and grain size affect the dynamics of a starting jet. As the focus of this paper is on the dynamic evolution of particle exit velocity, the following conclusions can be drawn. Maximum PEV shows

1. negative correlation with tube length;
2. positive correlation with particle load;
3. positive correlation with flaring vent walls, with peaks for funnel 15;
4. positive correlation with temperature; and
5. negative correlation with particle size.

Moreover, the temporal evolution of the velocity at which subsequent particles are being ejected shows the following:

1. The decay is nonlinear and it is primarily affected by particle load and tube length. The four setups used show very different trends. Results of experiments with setups 1, 1b, and 3 can be fitted by power law equations, results of experiments with setup 2 by an exponential equation. This is related to the height of the sample inside the autoclave as the uppermost part of the clasts is exposed to more permeable gas flow. Setup 3 presents the steepest velocity decay. As the smaller volume of gas and particles is located closer to the exit, the decompression is acting more rapidly.
2. Vent geometry only exerts a large effect in experiments performed with setup 2 and the nozzle vent geometry.
3. Temperature and particle size do not exhibit large effects.

Although natural volcanic eruptions are highly dynamic and the geometry of the plumbing system undoubtedly more complex than in these experiments, the effect of boundary conditions such as tube length (=conduit length) and particle load (=ejected mass) has been demonstrated to be first-order control on the ejection dynamics of particles not coupled with the gas ($St \gg 1$). On the other hand, the effect of vent geometry, temperature, and GSD was found to be of second-order control at our experimental conditions. For furthering

our understanding of eruptions, the coupling of expanding gas and particles under less regular geometries, choked-flow, and smaller St number conditions deserves further attention. In that context, the fragmentation depth from where particles are being accelerated and eventually ejected is a prime goal as we anticipate that it has strong implications for the assessment of volcanic ballistic hazards.

Appendix A

In this section, we present the GSD of the samples before decompression and the comparison of the effect of vent geometry on velocity decay for the conditions not presented in the main text. Figure A1 shows the grain size distribution of the used fragmental samples; Figure A2 shows the results of experiments performed with particles 1–2 mm, 500°C; and Figures A3 and A4 show the experiments with 0.5–1 mm particles, room temperature, and 500°C, respectively.

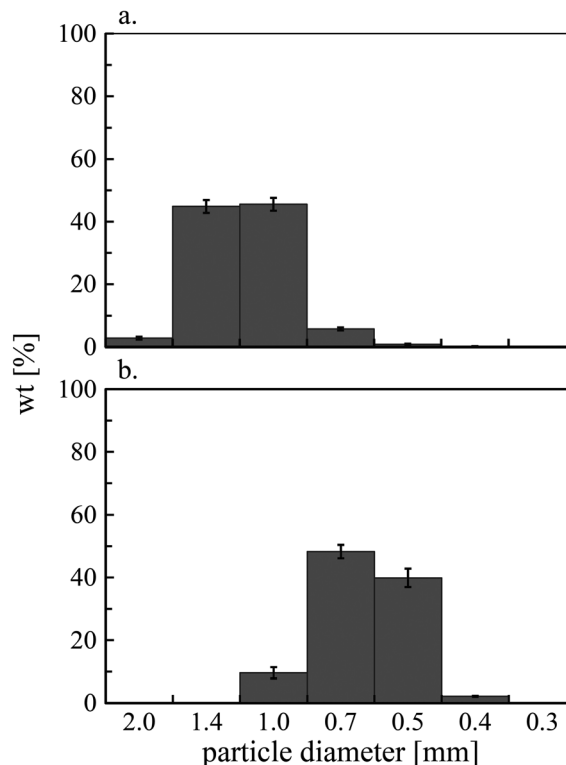


Figure A1. Grain size distribution before decompression plots of the (a) 1–2 mm and (b) 0.5–1 mm samples, respectively.

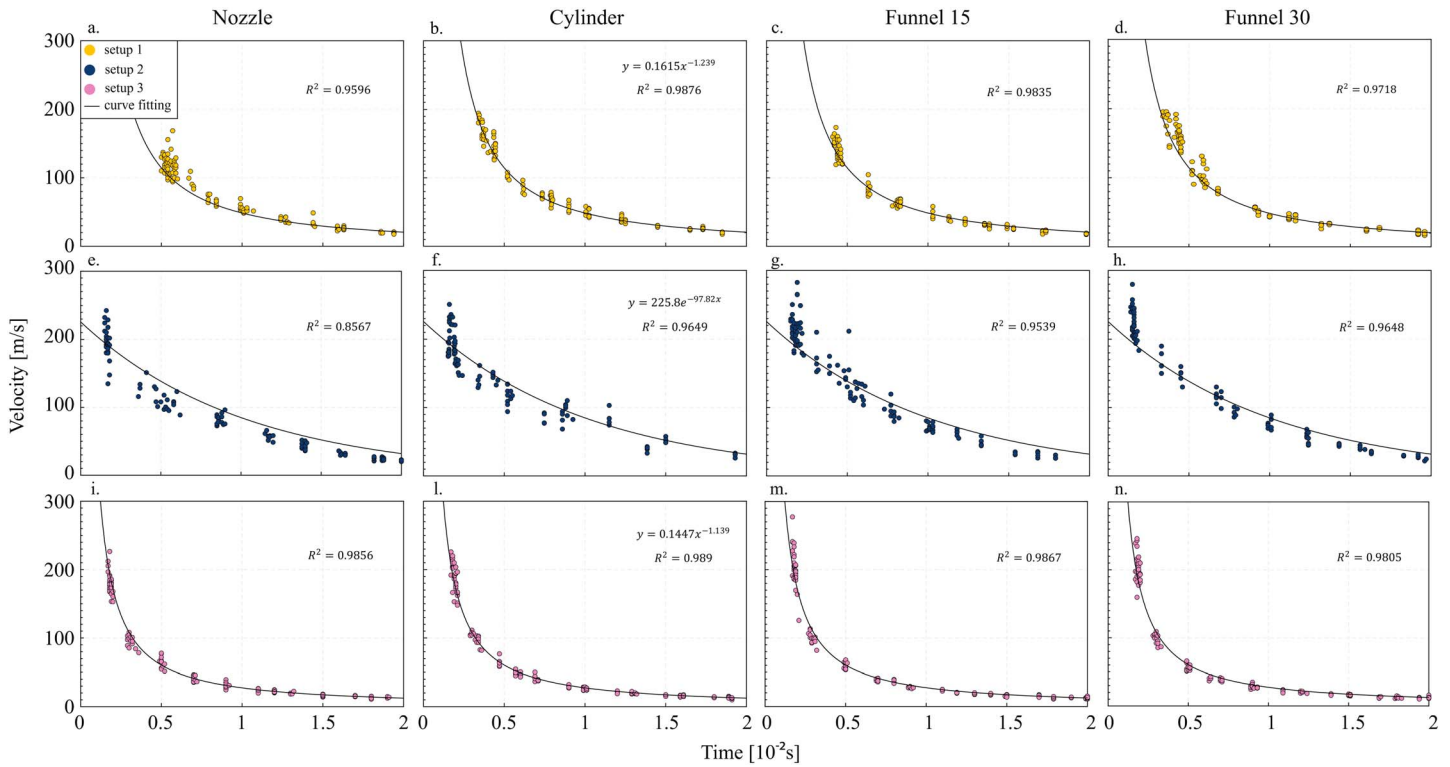


Figure A2. Particle jet velocity decay with time is shown for the four different vent geometries and setups, SL 1–2 mm particles, 15 MPa, 500°C. The curve fitting obtained for the cylinder vent case, equations can be found on the relative chart, is superimposed on the data from the other vents.

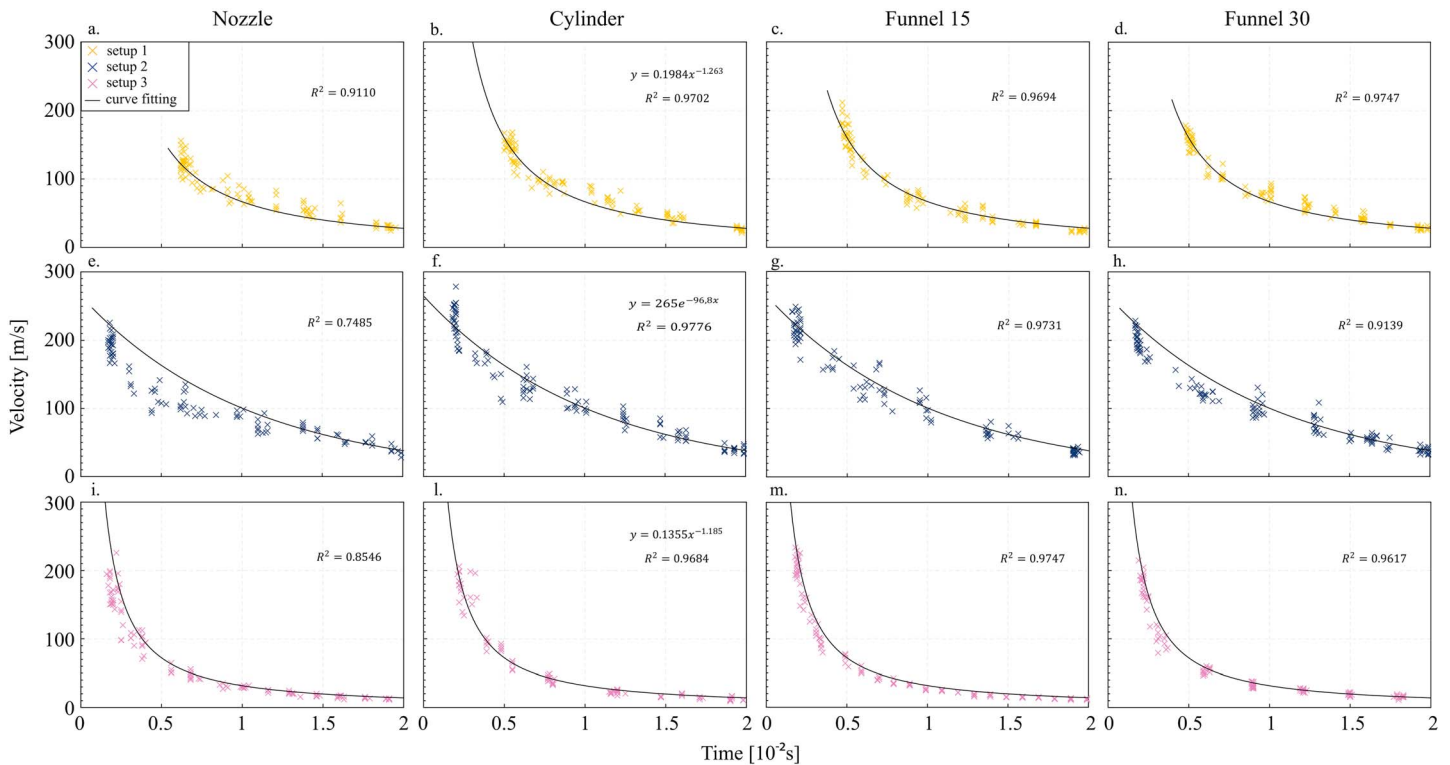


Figure A3. Particle jet velocity decay with time is shown for the four different vent geometries and setups, SL 0.5–1 mm particles, 15 MPa, room temperature. The curve fitting obtained for the cylinder vent case, equations can be found on the relative chart, is superimposed on the data from the other vents.

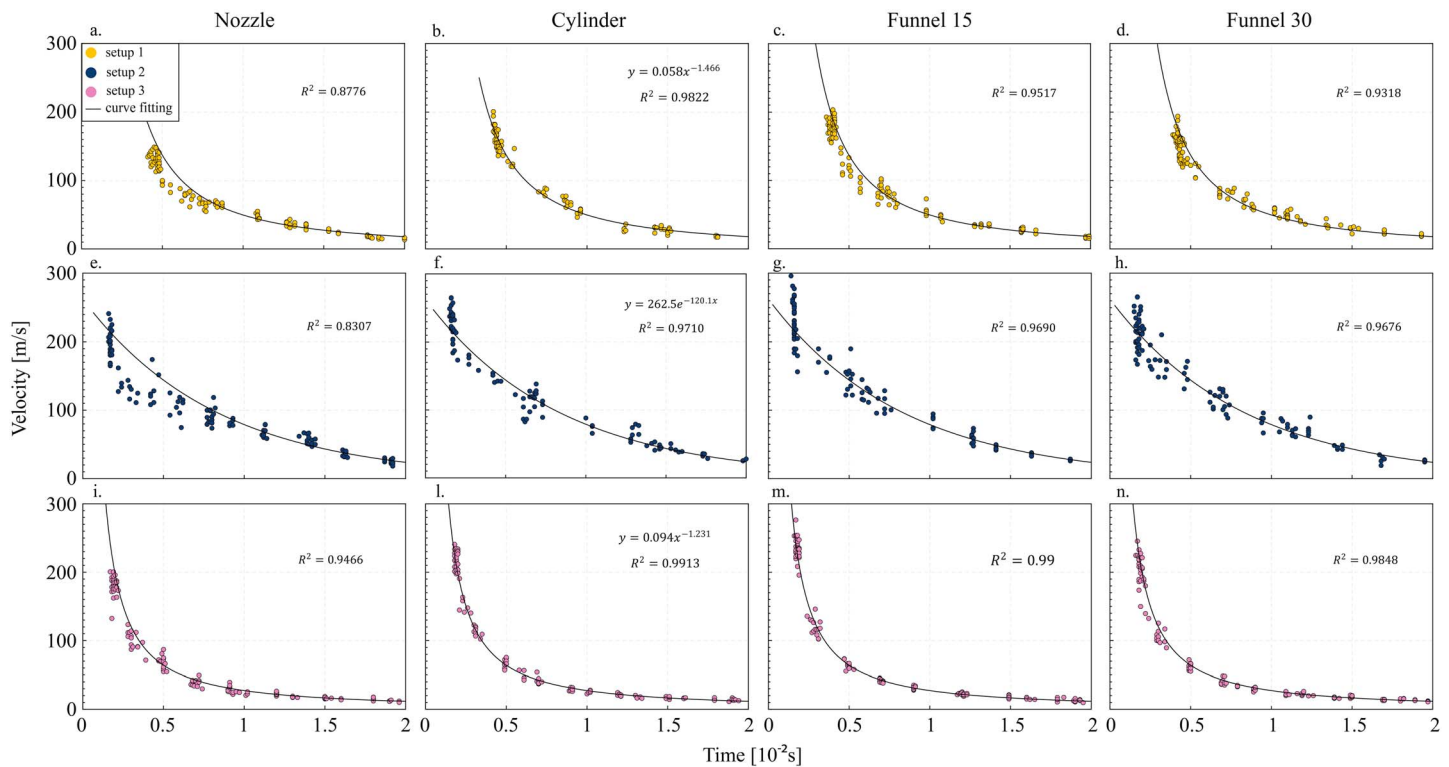


Figure A4. Particle jet velocity decay with time is shown for the four different vent geometries and setups, SL 0.5–1 mm particles, 15 MPa, 500°C. The curve fitting obtained for the cylinder vent case, equations can be found on the relative chart, is superimposed on the data from the other vents.

Acknowledgments

This work is fully supported by the VERTIGO Marie Curie ITN, funded through the European Seventh Framework Programme (FP7 2007–2013) under grant agreement 607905. Special thanks go to the technical staff of the LMU workshop, in particular Markus Siebe and Wolfgang Poppe. All particles used in the experiments have been generously offered by Link Baustoffe in Kretz (Germany). We thank Stefano Alois and Steffen Nitsch for their helpful comments and Fabian Wadsworth for the calorimetry measures. We thank Editor Michael Walter and two anonymous reviewers for their comments, which helped us in improving this manuscript. D.B.D. acknowledges support of ERC Advanced grant 247076 (EVOKES). A complete list of the experiments performed together with data measured and used to create the figures in the text are available in the supporting information of the paper. Additional information are available upon request at LMU Munich—Section of Mineralogy, Petrology, and Geochemistry and the corresponding author.

References

- Alatorre-Ibargüengoitia, M. A., B. Scheu, D. B. Dingwell, H. Delgado-Granados, and J. Taddeucci (2010), Energy consumption by magmatic fragmentation and pyroclast ejection during Vulcanian eruptions, *Earth Planet. Sci. Lett.*, *291*(1–4), 60–69, doi:10.1016/j.epsl.2009.12.051.
- Alatorre-Ibargüengoitia, M. A., B. Scheu, and D. B. Dingwell (2011), Influence of the fragmentation process on the dynamics of Vulcanian eruptions: An experimental approach, *Earth Planet. Sci. Lett.*, *302*(1–2), 51–59, doi:10.1016/j.epsl.2010.11.045.
- Alidibirov, M. A., and D. B. Dingwell (1996a), An experimental facility for the investigation of magma fragmentation by rapid decompression, *Bull. Volcanol.*, *58*(5), 411–416, doi:10.1007/s004450050149.
- Alidibirov, M. A., and D. B. Dingwell (1996b), Magma fragmentation by rapid decompression, *Lett. Nat.*, *380*, 146–148, doi:10.1038/380146a0.
- Bercovici, D., and C. Michaut (2010), Two-phase dynamics of volcanic eruptions: Compaction, compression and the conditions for choking, *Geophys. J. Int.*, *182*(2), 843–864, doi:10.1111/j.1365-246X.2010.04674.x.
- Burgisser, A., G. W. Bergantz, and R. E. Breidenthal (2005), Addressing complexity in laboratory experiments: The scaling of dilute multiphase flows in magmatic systems, *J. Volcanol. Geotherm. Res.*, *141*(3–4), 245–265, doi:10.1016/j.jvolgeores.2004.11.001.
- Capponi, A., J. Taddeucci, P. Scarlato, and D. M. Palladino (2016), Recycled ejecta modulating Strombolian explosions, *Bull. Volcanol.*, *78*(2), 1–13, doi:10.1007/s00445-016-1001-z.
- Carcano, S., L. Bonaventura, T. Esposti Ongaro, and A. Neri (2013), A semi-implicit, second order accurate numerical model for multiphase underexpanded volcanic jets, *Geosci. Model Dev. Discuss.*, *6*(1), 399–452, doi:10.5194/gmdd-6-399-2013.
- Carcano, S., T. Esposti Ongaro, L. Bonaventura, and A. Neri (2014), Influence of grain-size distribution on the dynamics of underexpanded volcanic jets, *J. Volcanol. Geotherm. Res.*, *285*, 60–80, doi:10.1016/j.jvolgeores.2014.08.003.
- Cerminara, M., T. Esposti Ongaro, and A. Neri (2016), Large eddy simulation of gas-particle kinematic decoupling and turbulent entrainment in volcanic plumes, *J. Volcanol. Geotherm. Res.*, *326*, 143–171, doi:10.1016/j.jvolgeores.2016.06.018.
- Chojnicki, K., A. B. Clarke, and J. C. Phillips (2006), A shock-tube investigation of the dynamics of gas-particle mixtures: Implications for explosive volcanic eruptions, *Geophys. Res. Lett.*, *33*, L15309, doi:10.1029/2006GL026414.
- Chojnicki, K. N., A. B. Clarke, J. C. Phillips, and R. J. Adrian (2015), The evolution of volcanic plume morphology in short-lived eruptions, *Geology*, *43*(8), 707–710, doi:10.1130/G36642.1.
- Clarke, A. B. (2013), Unsteady explosive activity: Vulcanian eruptions, in *Modeling Volcanic Processes—The Physics and Mathematics of Volcanism*, edited by S. A. Fagents et al., pp. 129–152, Cambridge Univ. Press, Cambridge, U. K.
- Douillet, G. A., K. R. Rasmussen, U. Kueppers, D. Lo Castro, J. P. Merrison, J. J. Iversen, and D. B. Dingwell (2014), Saltation threshold for pyroclasts at various bed-slopes: Wind tunnel measurements, *J. Volcanol. Geotherm. Res.*, *278*–279, 14–24, doi:10.1016/j.jvolgeores.2014.03.011.
- Dubosclard, G., F. Donnadieu, P. Allard, R. Cordesses, C. Hervier, M. Coltelli, and J. Kornprobst (2004), Doppler radar sounding of volcanic eruption dynamics at Mount Etna, *Bull. Volcanol.*, *66*(5), 443–456, doi:10.1007/s00445-003-0324-8.
- Elghobashi, S., and G. C. Truesdell (1993), On the two-way interaction between homogeneous turbulence and dispersed solid particles. I: Turbulence modification, *Phys. Fluids A*, *5*(7), 1790–1801, doi:10.1063/1.858854.

- Gaudin, D., J. Taddeucci, P. Scarlato, M. Moroni, C. Freda, M. Gaeta, and D. M. Palladino (2014), Pyroclast tracking velocimetry illuminates bomb ejection and explosion dynamics at Stromboli (Italy) and Yasur (Vanuatu) volcanoes, *J. Geophys. Res. Solid Earth*, *119*, 5384–5397, doi:10.1002/2014JB011096.
- Gouhier, M., and F. Donnadieu (2011), Systematic retrieval of ejecta velocities and gas fluxes at Etna volcano using L-band Doppler radar, *Bull. Volcanol.*, *73*(9), 1139–1145, doi:10.1007/s00445-011-0500-1.
- Jessop, D. E., J. Gilchrist, A. M. Jellinek, and O. Roche (2016), Are eruptions from linear fissures and caldera ring dykes more likely to produce pyroclastic flows?, *Earth Planet. Sci. Lett.*, *454*, 142–153, doi:10.1016/j.epsl.2016.09.005.
- Kieffer, S. W. (1984), Factors governing the structure of volcanic jets, in *Explosive Volcanism: Inception, Evolution, and Hazards*, edited by F. R. Boyd, pp. 143–157, Natl. Acad. Press, Washington, D. C.
- Kieffer, S. W. (1989), Geologic nozzles, *Rev. Geophys.*, *27*(1), 3–38, doi:10.1029/RG027i001p00003.
- Kieffer, S. W., and B. Sturtevant (1984), Laboratory studies of volcanic jets, *J. Geophys. Res.*, *89*(B10), 8253–8268, doi:10.1029/JB089iB10p08253.
- Koyaguchi, T., and A. W. Woods (1996), On the formation of eruption columns following explosive mixing of magma and surface-water, *J. Geophys. Res.*, *101*(B3), 5561–5574, doi:10.1029/95JB01687.
- Koyaguchi, T., Y. J. Suzuki, and T. Kozono (2010), Effects of the crater on eruption column dynamics, *J. Geophys. Res.*, *115*, B07205, doi:10.1029/2009JB007146.
- Kueppers, U., and F. B. Wadsworth (2015), What can pyroclastic deposits really tell us?, paper presented at the 26th IUGG conference, Prague, Czech Republic.
- Kueppers, U., D. Perugini, and D. B. Dingwell (2006a), “Explosive energy” during volcanic eruptions from fractal analysis of pyroclasts, *Earth Planet. Sci. Lett.*, *248*(3–4), 800–807, doi:10.1016/j.epsl.2006.06.033.
- Kueppers, U., B. Scheu, O. Spieler, and D. B. Dingwell (2006b), Fragmentation efficiency of explosive volcanic eruptions: A study of experimentally generated pyroclasts, *J. Volcanol. Geotherm. Res.*, *153*(1–2), 125–135, doi:10.1016/j.jvolgeores.2005.08.006.
- Montanaro, C., S. Scheu, K. Mayer, G. Orsi, R. Moretti, R. Isaia, and D. B. Dingwell (2016), Experimental investigations on the explosivity of steam-driven eruptions: A case study of Solfatara volcano (Campi Flegrei), *J. Geophys. Res. Solid Earth*, *121*, 7996–8014, doi:10.1002/2016JB013273.
- Ogden, D. (2011), Fluid dynamics in explosive volcanic vents and craters, *Earth Planet. Sci. Lett.*, *312*(3–4), 401–410, doi:10.1016/j.epsl.2011.10.032.
- Peña Fernández, J. J., and J. Sesterhenn (2017), Compressible starting jet: Pinch-off and vortex ring–trailing jet interaction, *J. Fluid Mech.*, *817*, 560–589, doi:10.1017/jfm.2017.128.
- Saad, M. (1985), *Compressible Fluid Flow*, 570 pp., Prentice-Hall, Inc., Englewood Cliffs, N. J.
- Saffaraval, F., S. A. Solovitz, D. E. Ogden, and L. G. Mastin (2012), Impact of reduced near-field entrainment of overpressured volcanic jets on plume development, *J. Geophys. Res.*, *117*, B05209, doi:10.1029/2011JB008862.
- Scharff, L., M. Hort, and N. R. Varley (2015), Pulsed Vulcanian explosions: A characterization of eruption dynamics using Doppler radar, *Geology*, *43*(11), 995–998, doi:10.1130/G36705.1.
- Solovitz, S. A., D. E. Ogden, D. Kim, and S. Y. Kim (2014), Coupled fluid and solid evolution in analogue volcanic vents, *J. Geophys. Res. Solid Earth*, *119*, 5342–5355, doi:10.1002/2014JB010993.
- Sommerfeld, M. (1994), The structure of particle-laden, underexpanded free jets, *Shock Waves*, *3*(4), 299–311, doi:10.1007/BF01415828.
- Taddeucci, J., P. Scarlato, A. Capponi, E. Del Bello, C. Cimarelli, D. M. Palladino, and U. Kueppers (2012), High-speed imaging of Strombolian explosions: The ejection velocity of pyroclasts, *Geophys. Res. Lett.*, *39*, L02301, doi:10.1029/2011GL050404.
- Taddeucci, J., M. A. Alatorre-Ibarguengoitia, D. M. Palladino, P. Scarlato, and C. Camaldo (2015), High-speed imaging of Strombolian eruptions: Gas-pyroclast dynamics in initial volcanic jets, *Geophys. Res. Lett.*, *42*, 6253–6260, doi:10.1002/2015GL064874.
- Tournigand, P. Y., J. J. Peña Fernández, J. Taddeucci, D. Perugini, and J. Sesterhenn (2017), Fractal analysis: A new tool in transient volcanic ash plume characterization, paper presented at the EGU General Assembly 2017 conference, Vienna, Austria. Abstract number: Vol. 19, EGU2017–14643.
- Turner, N., B. Houghton, J. Taddeucci, J. von der Lieth, U. Kueppers, D. Gaudin, T. Ricci, K. Kim, and P. Scarlato (2017), Peering into open volcanic vents, *Eos. Trans. AGU*.
- Valentine, G. A. (1998), Eruption column dynamics, in *From Magma to Tephra*, edited by A. Freundt and M. Rosi, pp. 91–138, Elsevier, Amsterdam, Netherlands.
- Wadsworth, F. B., J. Vasseur, B. Scheu, J. E. Kendrick, Y. Lavallée, and D. B. Dingwell (2016), Universal scaling for fluid permeability during volcanic welding and sediment diagenesis, *Geology*, *44*(3), 219–222, doi:10.1130/G37559.
- Waples, D. W., and J. S. Waples (2004), A review and evaluation of specific heat capacities of rocks, minerals, and subsurface fluids. Part 1: Minerals and nonporous rocks, *Nat. Resour. Res.*, *13*(2), 97–122, doi:10.1023/B:NARR.0000032647.41046.e7.
- Wilson, L., and J. W. Head (1981), Ascent and eruption of basaltic magma on the Earth and Moon, *J. Geophys. Res.*, *86*(B4), 2971–3001, doi:10.1029/JB086iB04p02971.
- Wilson, L., R. S. J. Sparks, and G. P. L. Walker (1980), Explosive volcanic eruptions—IV. The control of magma properties and conduit geometry on eruption column behaviour, *Geophys. J. R. Astron. Soc.*, *63*, 117–148, doi:10.1111/j.1365-246X.1980.tb02613.x.
- Woods, A. W. (1988), The fluid dynamics and thermodynamics of eruption columns, *Bull. Volcanol.*, *50*(3), 169–193, doi:10.1007/BF01079681.
- Woods, A. W. (1995), A model of Vulcanian explosions, *Nucl. Eng. Des.*, *155*(1–2), 345–357, doi:10.1016/0029-5493(94)00881-X.
- Woods, A. W., and S. M. Bower (1995), The decompression of volcanic jets in a crater during explosive volcanic eruptions, *Earth Planet. Sci. Lett.*, *131*(3–4), 189–205, doi:10.1016/0012-821x(95)00012-2.
- Yin, S., M. Meyer, W. Li, H. Liao, and R. Lupoi (2016), Gas flow, particle acceleration, and heat transfer in cold spray: A review, *J. Therm. Spray Technol.*, *25*(5), 874–896, doi:10.1007/s11666-016-0406-8.